Conformal Li_2HfO_3/HfO_2 Nanoparticle Coatings on Layered Ni-Rich Oxide Cathodes for Stabilizing Interfaces in All-Solid-State Batteries

Ruizhuo Zhang,[a] Yuan Ma,[a,†,*] Yushu Tang,[b,c] Damian Goonetilleke,[a,‡] Thomas Diemant,[d] Jürgen Janek,[a,e] Aleksandr Kondrakov,[a,f] and Torsten Brezesinski[a,*]

[a] Battery and Electrochemistry Laboratory (BELLA), [b] Institute of Nanotechnology, Karlsruhe Institute of Technology (KIT), Hermann-von-Helmholtz-Platz 1, 76344 Eggenstein-Leopoldshafen, Germany

[c] Karlsruhe Nano Micro Facility (KNMFi), Karlsruhe Institute of Technology (KIT), Hermann-von-Helmholtz-Platz 1, 76344 Eggenstein-Leopoldshafen, Germany

[d] Helmholtz Institute Ulm (HIU) Electrochemical Energy Storage, Helmholtzstr. 11, 89081 Ulm, Germany

[e] Institute of Physical Chemistry and Center for Materials Research (ZfM/LaMa), Justus-Liebig-University Giessen, Heinrich-Buff-Ring 17, 35392 Giessen, Germany.

[f] BASF SE, Carl-Bosch-Str. 38, 67056 Ludwigshafen, Germany

* Corresponding authors: yuan.ma@seu.edu.cn, torsten.brezesinski@kit.edu

[†] Current affiliation: Key Laboratory of Energy Thermal Conversion and Control of Ministry of Education, School of Energy and Environment, Southeast University, Nanjing 211189, Jiangsu, China

[‡] Current affiliation: Umicore Corporate Research & Development, Watertorenstraat 33, 2250 Olen, Belgium

Abstract

Solid-state batteries (SSBs) are a promising next-generation energy-storage solution to complement or replace current battery technologies in the wave of automotive electrification. Especially SSBs using sulfide solid electrolytes (SEs) hold great potential; however, (electro)chemical instability when in contact with layered oxide cathode active materials (CAMs) remains an obstacle to further implementation. SE degradation occurring during cycling adversely affects the ion/electron transport and may possibly cause mechanical failure. In the present work, a protective surface coating composed of Li_2HfO_3 and HfO_2 nanoparticles (NPs) was produced on the secondary particles of a high-capacity $LiNi_{0.85}Co_{0.1}Mn_{0.05}O_2$ CAM to mitigate side reactions and enable robust interfacial charge transfer. HfO_2 NPs dispersed in solution served both as coating material and as precursor to react with residual lithium during post-deposition annealing. The Li_2HfO_3/HfO_2-coated NCM85 showed much improved cycling performance over bare CAM in all-inorganic SSB cells with Li_6PS_5Cl SE and $Li_4Ti_5O_{12}$ anode. Thorough characterization using a series of techniques helped to elucidate the role that the coating plays in stabilizing interfaces and preserving structural integrity of the cathode.

Introduction

While extensive investigation and commercialization of lithium-ion batteries have made the electrification of automobiles possible, the intrinsic flammability of (ordinary) organic, liquid electrolytes and dendrite formation associated with the lithium-metal anode pose safety concerns and challenges to fast charging.[1-5] Therefore, considerable attention is directed towards solid-state batteries (SSBs), particularly those using layered Ni-rich oxide cathode active materials (CAMs), e.g. $LiNi_xCo_yMn_zO_2$ (NCM or NMC) or $LiNi_xCo_yAl_zO_2$ (NCA) (with $x + y + z = 1$ and $x \geq 0.8$),[6] and superionic thiophosphate solid electrolytes (SEs) such as Li_6PS_5X (with X = Cl, Br, I),[7] Li_3PS_4,[8] $Li_7P_3S_{11}$[9] or $Li_{9.54}Si_{1.74}P_{1.44}S_{11.7}Cl_{0.3}$,[10] to name a few. The latter materials exhibit a high ionic conductivity at room temperature and are mechanically soft, allowing for facile processing by cold pressing.

Despite the individual advantages of Ni-rich NCM CAMs and sulfide SEs, their practical combination in SSBs is faced with many challenges. The stability of NCM decreases with increasing Ni content, while residual lithium species and cation intermixing (Ni^{2+} on lithium site) impair ion transport.[11] Apart from that, the charge cutoff voltage of NCM cells surpasses the electrochemical stability window of sulfide SEs.[12-14] As a result, the NCM|SE interface suffers from degradation, resulting in impedance buildup. In addition, oxygen released from the CAM (near) surface at high states of charge exacerbates the degradation. It further causes the formation of redox-inactive NiO-like rock salt phases, which accelerates the capacity fading.[15-17] Notably, recent reports revealed that the

performance decay of NCM/sulfide SE battery systems is also due in part to mechanical failure. This includes particle fracture and contact loss caused by “breathing” of the NCM particles during cycling and interfacial side reactions.[18,19]

A viable approach for solving the aforementioned issues is fabricating a protective coating on the NCM particles, with the objective to prevent physical contact between the bare CAM and the sulfide SE. In recent years, various coating materials have been reported, including binary oxides (e.g. ZrO_2,[20,21] HfO_2,[22,23] Al_2O_3,[24] Li_2O-ZrO_2[25,26]) and lithium-based ternary oxides (e.g. $LiNbO_3$,[27,28] $LiAlO_2$,[29] $LiZrO_3$,[28,30] $Li_4Ti_5O_{12}$[31]). It should be noted though that the coating process inevitably induces the formation of some impurities, especially carbonates, on the CAM surface.[20,27,30,32] In this regard, Jung *et al*. showed that Li_2CO_3 is detrimental to the lithium transport.[33] Furthermore, electrochemical oxidation of carbonates leads to the evolution of oxygen (in addition to CO_2) that can undergo unwanted follow-up reactions with other components in the electrode.[34,35] The limited stability of sulfide SEs, in general, may have a negative effect on the integrity of the coating structure/morphology (loosening/delamination of the surface layer etc.). Regardless, producing a conformal coating while preventing major carbonate formation is challenging. Nevertheless, the emerging solution-based nanoparticle (NP) coating technology has been shown to overcome non-uniformity problems, but it does not solve the carbonate formation issue (as demonstrated for ZrO_2 NPs as coating material).[20]

As a continuation to previous work,[20,23] here the original coating strategy was modified to address specifically the latter aspect. To produce well-defined coatings on the CAM primary/secondary particles, the NPs should be ideally monodisperse and present in a non-agglomerated state, i.e. completely dispersed in a solvent, which is challenging to achieve by most methods. HfO_2 was selected as coating material and precursor due to not only the possibility to readily prepare NP dispersions of good quality, but also because of its high stability when in contact with Ni-rich CAMs (irrespective of the degree of lithiation or, in other words, state of charge).[36,37] After applying the coating to the particles, the CAM, $LiNi_{0.85}Co_{0.1}Mn_{0.05}O_2$ (NCM85), was subject to annealing to initiate the reaction between HfO_2 and residual lithium. This procedure was meant to decrease the amount of surface carbonates and improve the ionic conductivity of the coating, even though the formed lithium-based ternary oxide is less stable than the parent material. The Li_2HfO_3/HfO_2-coated NCM85 (cathodes with high active material content and high areal loading) was eventually tested in bulk-type SSB cells with Li_6PS_5Cl (LPSCl) SE and $Li_4Ti_5O_{12}$ (LTO) anode and found to show improved cyclability over uncoated CAM.

Results and Discussion

A schematic of the two-step coating approach employed in the present work is shown in **Fig. 1a**. In short, non-agglomerated HfO_2 NPs (prepared by solvothermal synthesis)

dispersed in solution were combined with the pristine NCM85 (referred to as Bare-NCM85) for surface coating,[20,23] followed by annealing at 700 °C under oxygen. The second step led to partial formation of Li_2HfO_3 by solid-state reaction with the residual lithium present on the CAM surface, thereby generating a kind of hybrid coating composed of HfO_2 and Li_2HfO_3 (referred to as LHO-NCM85).

Powder X-ray diffraction (XRD) and subsequent Rietveld refinement analysis (see **Fig. 1b** and **Fig. S1**, Supporting Information) were used to probe the crystal structure before and after coating. The XRD pattern of LHO-NCM85 was found to be very similar to that of Bare-NCM85, suggesting that the layering is well preserved (*R*−3*m* space group; see structural model in **Fig. 1c**). From the refined structural parameters given in **Tab. S1**, it can be seen that LHO-NCM85 exhibits slightly larger *a* and *c* lattice parameters than Bare-NCM85, resulting in an increase in cell volume by about 0.05 Å^3. However, the degree of cation intermixing ($Ni_{Li}^{\bullet}$ defects) remained virtually unaltered, with 3.2% for Bare-NCM85 and 3.5% for LHO-NCM85, indicating that lattice lithium consumption during post-deposition annealing can be largely neglected.

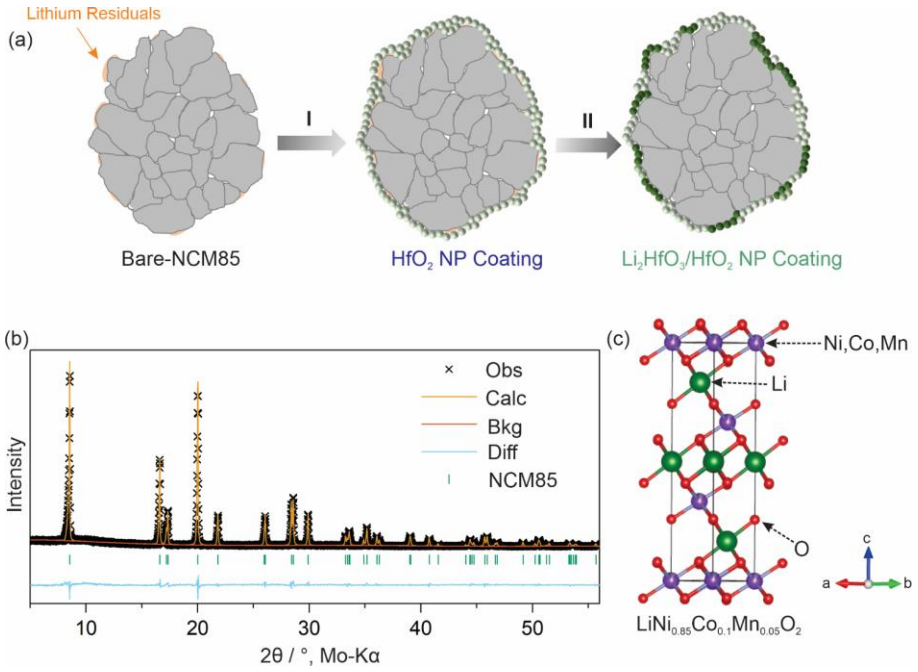

Figure 1. (a) Schematic of the coating procedure. (b) Powder XRD pattern and corresponding Rietveld refinement profile for LHO-NCM85. (c) Structural model of the NCM85.

The morphology of the Bare- and LHO-NCM85 CAMs was studied by means of scanning electron microscopy (SEM). The micrometer-sized secondary particles were more or less spherical in shape and consisted of sub-500 nm primary particles, see **Fig. 2a-d**. The surface of the individual primary particles and the grain boundaries in Bare-NCM85 were

clean and well defined. In contrast, LHO-NCM85 had rougher surfaces and fuzzy grain boundaries, with traces of NPs clearly covering the material and filling the gaps between the primary particles. In addition to SEM imaging, energy dispersive X-ray spectroscopy (EDS) mapping was used to characterize the coated CAM (see **Fig. 2e-i**), revealing an even distribution of Hf, Ni, Co, and Mn on the secondary particle level. From this data, it can be concluded that the surface of the NCM85 was uniformly coated considering the resolution limit of the technique.

Attenuated total reflection-infrared (ATR-IR) spectroscopy data collected from the Bare- and LHO-NCM85 samples (see **Fig. 2j**) displayed carbonate vibrational bands at 870, 1430, and 1490 cm^{-1}.[32,38] The bands observed for LHO-NCM85 were much weaker in intensity than that of Bare-NCM85. This difference implies a possible decomposition of Li_2CO_3 and/or chemical reaction with the HfO_2 NPs on the CAM surface. X-ray photoelectron spectroscopy (XPS) data for the Hf 4f core-level region (see **Fig. 2k**) revealed a total of two doublets after fitting. The doublet at higher binding energy (Hf $4f_{7/2}$ at 18.1 eV) can be assigned to Hf^{4+} in HfO_2,[39,40] while that at lower binding energy (Hf $4f_{7/2}$ at 15.6 eV) arises from the change in chemical environment due to lithium incorporation. A similar observation was made for Al_2O_3 coatings on NCM; new peaks appeared upon conversion to the respective lithium-based ternary oxide.[29,41] Overall, XPS analysis indicated that the coating is a mixture of HfO_2 and Li-Hf-O species.

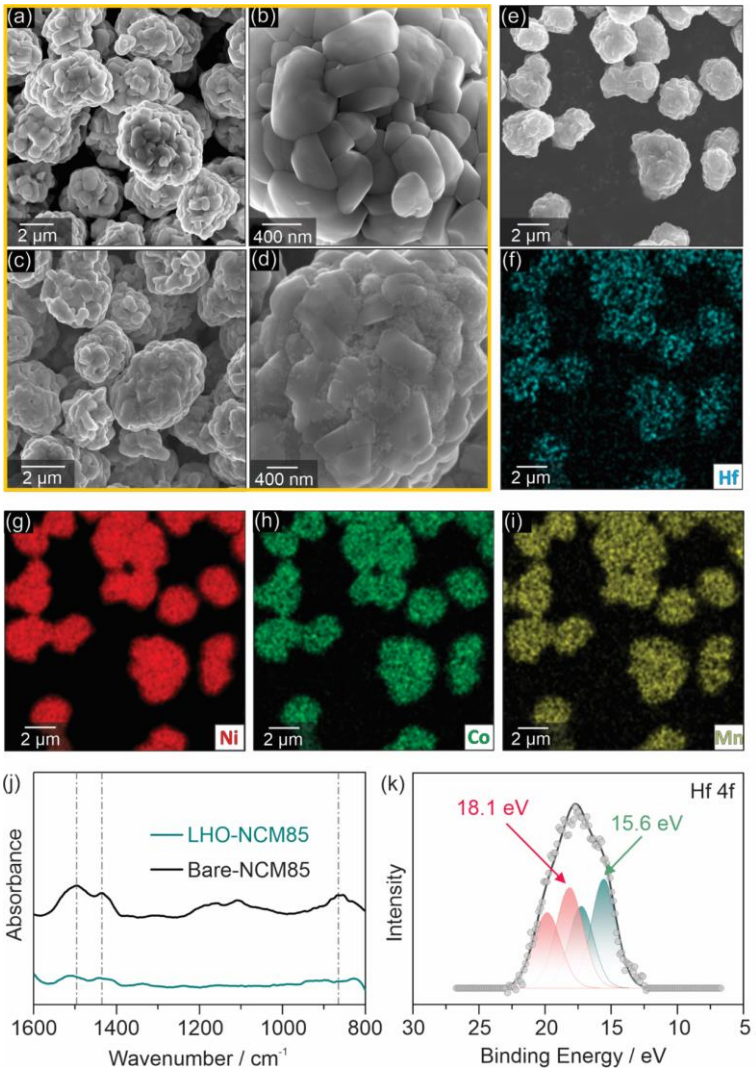

Figure 2. SEM images at different magnifications of (a, b) Bare-NCM85 and (c, d) LHO-NCM85. (e) Low-magnification SEM image of LHO-NCM85 and corresponding EDS mapping results for (f) Hf, (g) Ni, (h) Co, and (i) Mn. (j) ATR-IR data collected from the Bare-NCM85 and LHO-NCM85. Dashed lines denote the carbonate vibrational bands. (k) Hf 4f spectrum of LHO-NCM85.

High-angle annular dark-field scanning transmission electron microscopy (HAADF STEM) measurements were conducted on a focused ion beam (FIB)-prepared LHO-NCM85 specimen to gain more insights into the coating structure and composition. The low-magnification image in **Fig. 3a** demonstrates that the secondary particles were coated well with a shell-like layer. EDS mapping (see **Fig. 3b**) further confirmed the presence of a conformal coating of thickness ~12 nm. The data also indicate that hafnium interdiffusion into the subsurface volume or even the NCM85 bulk can be ruled out (unlike for sol-gel or atomic layer deposition (ALD)-derived zirconia coatings, for

example).[21,22,30,42] This result agrees with the cation intermixing from Rietveld refinement analysis, suggesting minor changes to the nickel on lithium site occupancy factor after post-deposition annealing. The high-resolution TEM (HR TEM) image in **Fig. 3c**, taken from a selected region of the coating, displays lattice fringes, indicating the nanocrystalline nature of the HfO_2 and Li-Hf-O species. The corresponding fast Fourier transform (FFT) pattern shown in **Fig. 3d** can be indexed to the monoclinic phase of HfO_2 ($P2_1/c$ space group, JCPDS card no. 34-0104) and monoclinic Li_2HfO_3 ($C2/m$ space group, mp-756597).[43] The electron energy loss (EEL) spectrum in **Fig. 3e** corroborates the presence of lithium in the coating (see Li K-edge peak at ~60 eV; note that the peaks in the energy loss range between 30 and 50 eV are characteristic of Hf) and therefore formation of a Li_2HfO_3/HfO_2 hybrid shell on the CAM surface.[44-46]

Taking into account the above results, quantitative XPS analysis (comparison of peak areas) revealed a ratio of Hf atoms in HfO_2 vs. Li_2HfO_3 ratio of 1.02. (see **Tab. S2**). Furthermore, inductively coupled plasma-optical emission spectroscopy (ICP-OES, see **Tab. S3**) showed a Hf content of 0.84 wt. %, which translates into a total coating content of 1.06 wt. % with 0.50 wt. % HfO_2 and 0.56 wt. % Li_2HfO_3. Because the intensity of the carbonate vibrational bands was strongly diminished for LHO-NCM85 and the degree of cation intermixing barely changed upon surface modification, it appears that Li_2CO_3 served as the major lithium source in the formation of Li_2HfO_3. Some more discussion on this (involving results from acid titration experiments) is provided in the Supporting Information.

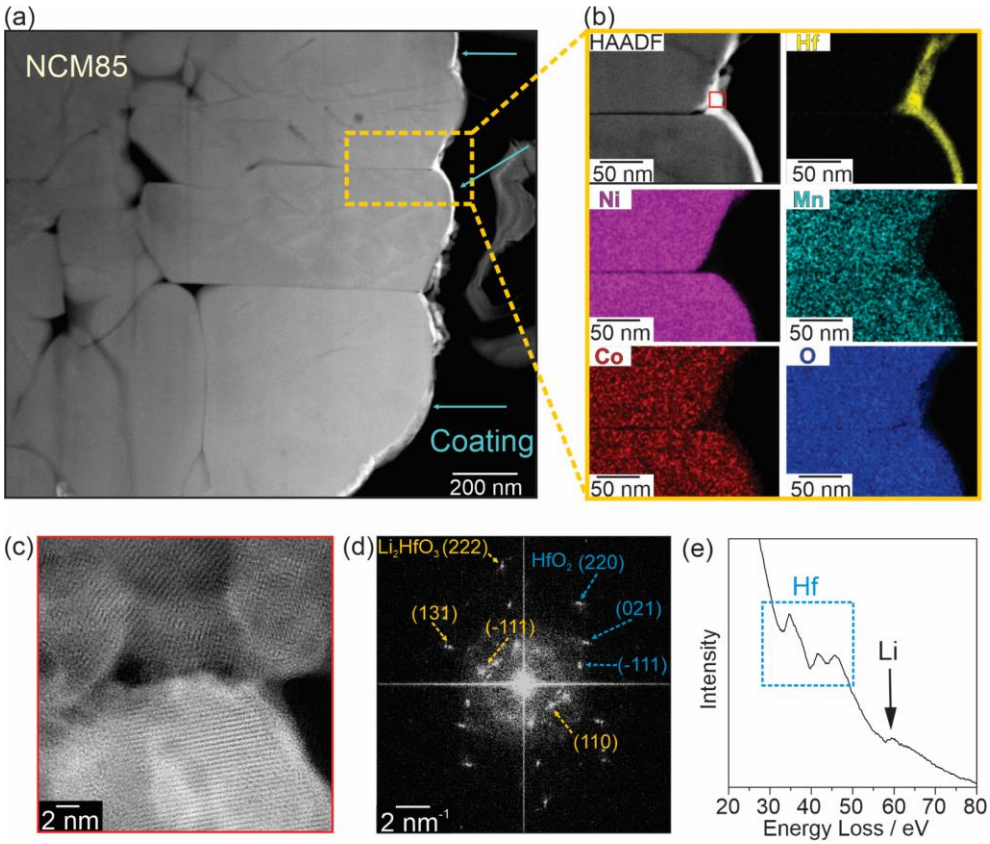

Figure 3. (a) Low-magnification HAADF STEM image of LHO-NCM85. (b) HAADF STEM image of the region denoted by the yellow box in (a) and corresponding EDS mapping of Hf, Ni, Mn, Co, and O. (c) HR TEM image of the surface coating denoted by the red box in (b), (d) corresponding FFT pattern, and (e) EEL spectrum.

To assess the effectiveness of the CAM coating, the cycling performance of LHO-NCM85 was examined in SSB full cells with a cathode loading of about 11 mg_{NCM85}/cm^2 (corresponding to ~3 mAh/cm^2 for q_{th} = 274 mAh/g) and compared to that of the uncoated reference material (Bare-NCM85). Argyrodite LPSCl was used as SE in the cathode and anode, and Super C65 carbon black served as conductive additive. The sandwich-type cell structure comprised three layers, namely CAM/LPSCl/C65|LPSCl|LTO/LPSCl/C65. The electrochemical testing was carried out at 45 °C and 81 MPa in the voltage range 1.35-2.75 V vs. $Li_4Ti_5O_{12}/Li_7Ti_5O_{12}$.

Fig. 4a shows voltage profiles of the initial cycle at 0.1C rate, revealing significant improvements in specific discharge capacity, with q_{dis} = 187 vs. 162 mAh/g, and Coulomb efficiency, with 82.4 vs. 78.6%, for cells using the LHO-NCM85. This is clearly due to the presence of the protective coating (modification/stabilization of the CAM|SE interface), which helps to mitigate adverse side reactions and therefore positively affects the charge transfer. The corresponding differential capacity (dq/dV) curves in **Fig. 4b** display the

phase transitions (from H1-M over M-H2 to H2-H3, with H: hexagonal and M: monoclinic) that the CAM undergoes during lithium extraction. These transitions are typical of Ni-rich NCM cathodes.[47] Notably, compared to LHO-NCM85, the H1-M peak of Bare-NCM85 appeared at a higher voltage (by 10 mV, see inset of **Fig. 4b**) because of sluggish kinetics. This result suggests that coating the secondary particles with an inert material is an effective means to reduce polarization, even at low C-rate.

Figs. 4c and **d** and **S2** compare the rate performance of the cells using bare and coated NCM85. Specifically, the C-rate was gradually increased from 0.1 to 1.0C. The LHO-NCM85 CAM delivered specific discharge capacities of 187, 155, 112, and 71 mAh/g at 0.1, 0.2, 0.5, and 1.0C, respectively, i.e. about 83, 60, and 38% of the capacity achieved at 0.1C was retained at the higher C-rates (see **Fig. 4e**). By contrast, in the case of Bare-NCM85, the specific discharge capacities were lower by about 25 mAh/g, independent of the C-rate. For example, only 28% (46 mAh/g) of the capacity was retained at 1.0C relative to that at 0.1C (162 mAh/g). This behavior can be explained by growing overpotential with increasing C-rate (see **Fig. 4c**), which was less pronounced in the LHO-NCM85-based cells due to the coating helping to stabilize the CAM|SE interface (see also **Fig. S3a-c** with related discussion).

Fig. 4f shows the long-term cyclability of both CAMs at a rate of 0.2C. Bare-NCM85 revealed accelerated capacity fading after around 50 cycles. This is due to (interfacial) impedance buildup during cycling resulting from the SE decomposition and mechanical degradation caused by particle fracture and void formation.[18,48] Note that especially the latter exacerbates the deterioration of electronic/ionic percolation through the composite cathode.[19] As a result, the capacity retention after 200 cycles was only 45.4%. Unlike Bare-NCM85, the LHO-NCM85-based cells showed a much more stable performance, with 81.4% of the initial capacity retained after the same number of cycles. The average Coulomb efficiency also improved from about 99.5% for Bare-NCM85 to 99.7% for LHO-NCM85.

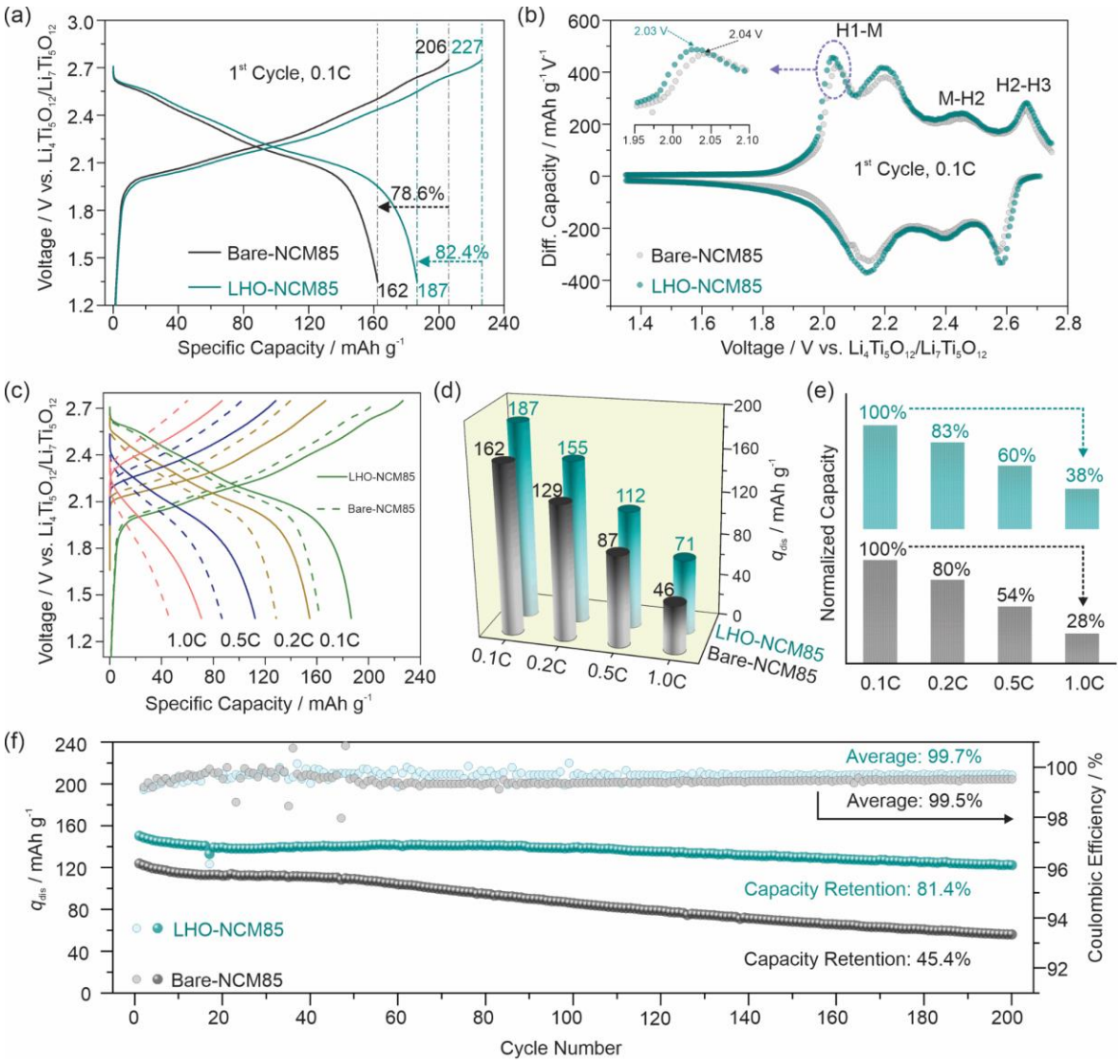

Figure 4. Cyclability of the Bare- and LHO-NCM85 CAMs in pellet-stack SSB full cells at 45 °C. (a) First-cycle voltage profiles and (b) differential capacity curves at 0.1C. (c) Voltage profiles at different C-rates and (d) corresponding specific discharge capacities. (e) Capacity retention with respect to 0.1C cycling (set to 100%). (f) Long-term cycling performance at 0.2C.

The differential capacity plots of selected cycles in **Fig. 5a** and **b** (from the long-term cycling tests shown in **Fig. 4f**) provide more information about the structural evolution of the NCM85 during cell operation. Characteristic peaks referring to the aforementioned phase transitions were evident for both CAMs in the beginning of cycling. As can be seen from the data, the polarization was much lower for LHO-NCM85 after 200 cycles. In particular, the H1-M peak was shifted to higher voltages by about 60 mV in the case of Bare-NCM85, compared to less than 10 mV for LHO-NCM85 (from the 10th cycle onward).

This suggests that the protective coating is somewhat capable of suppressing adverse side reactions in the later cycles, eventually leading to improvements in CAM|SE interface stability.[49] The decrease in H1-M peak intensity/area for Bare-NCM85 is indicative of severe loss of lithium inventory.[50] The reason for this is likely a combination of electrochemical and mechanical degradation, including intergranular cracking of the NCM85 secondary particles and contact loss between CAM and SE. The coating, apparently, cannot only mitigate degradation at the CAM|SE interface but also ensure structural integrity of the cathode, which is ultimately reflected in enhanced cyclability.

To corroborate the relationship between microstructural evolution and electrochemical performance, the structure/morphology of the Bare- and LHO-NCM85 particles before and after cycling was probed using SEM (see top view and cross-sectional images in **Fig. 5c**-**j**). In pristine state, the CAM secondary particles, indicated by yellow arrows in the respective images, were well embedded in the SE matrix at the micrometer level. After 200 cycles, particle fracture was clearly visible for the Bare-NCM85 cathode (see red circles in **Fig. 5g**), while the LHO-NCM85 particles appeared to be largely intact (see **Fig. 5h**). However, some SE cracking and void formation was evident in both cathodes. Furthermore, subtle differences in the cross-sectional SEM images collected from the Bare- and LHO-NCM85 cathodes after cycling (see **Fig. 5i** and **j**) seem to indicate different levels of interphase formation, yet this needs further study. We note that a recent work demonstrated that mechanical degradation is exacerbated by interfacial SE decomposition.[23,51] In addition, mobile sulfur species may diffuse into the intergranular cracks, thus further increasing degradation.[23,52,53]

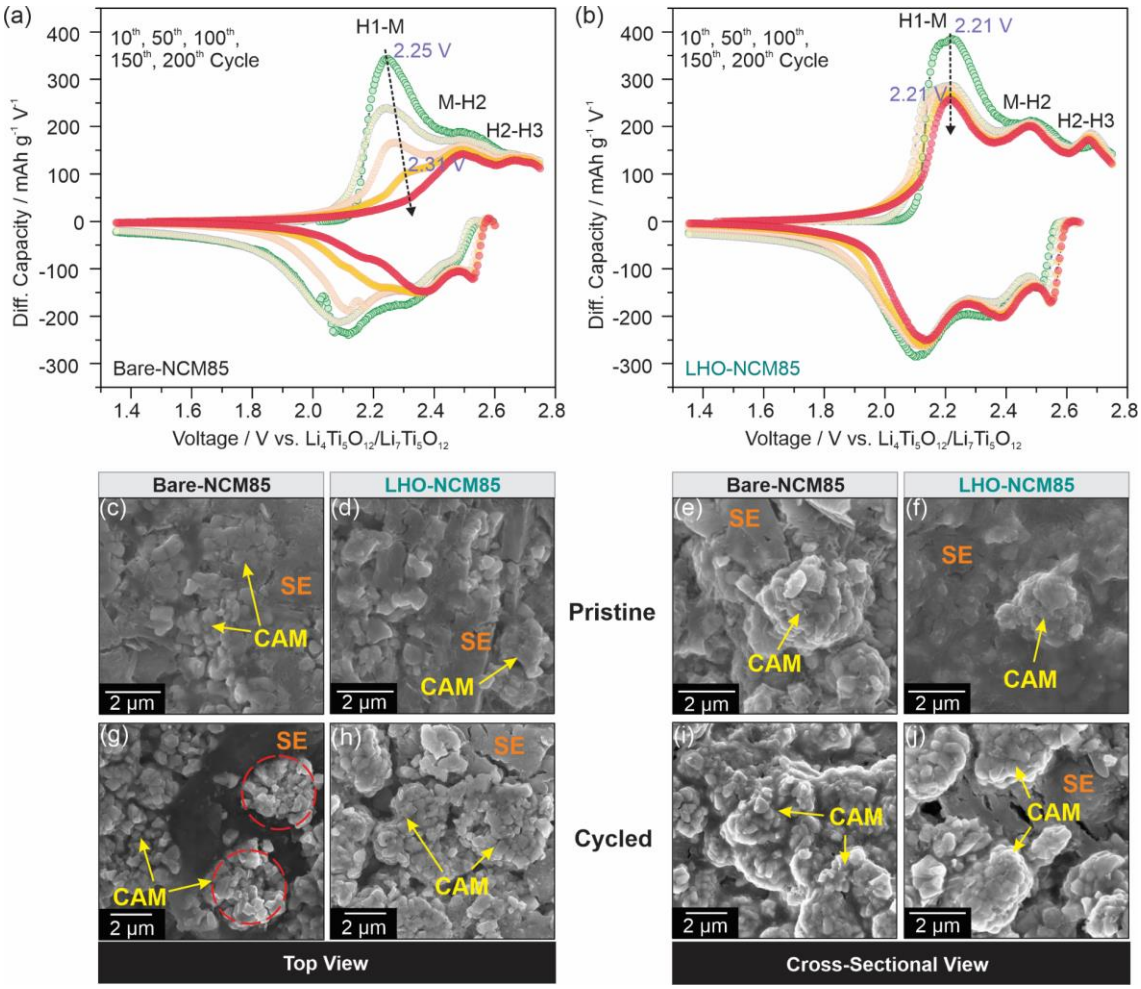

Figure 5. Differential capacity curves of selected cycles from **Fig. 4f** for (a) Bare-NCM85 and (b) LHO-NCM85. (c-j) Top view and cross-sectional SEM images of the Bare-NCM85 and LHO-NCM85 cathodes in pristine state and after 200 cycles at 0.2C.

To confirm the apparent differences in (decomposition) interphase formation among the Bare-NCM85 and LHO-NCM85 CAMs, XPS measurements were conducted on the cycled cathodes, with emphasis placed on the S 2p and P 2p core-level regions. The experimental data are shown in **Fig. S4a**. Pristine LPSCl (reference) revealed three doublets at binding energies of 160.1/161.3 eV, 161.5/162.7 eV, and 163.6/164.8 eV in the S 2p spectrum, which can be assigned to free S^{2-} and/or Li_2S, PS_4^{3-}, and polysulfides (oxidized sulfur), respectively.[23,54,55] In the P 2p region, the main doublet was located at 132.1 eV (P $2p_{3/2}$ peak). For the cycled Bare- and LHO-NCM85 cathodes, the intensity of the doublet at 163.6 eV (S $2p_{3/2}$) was strongly increased. In addition, new doublets appeared at higher binding energies (>167.1 eV), originating from side reactions between the CAM and SE particles and leading to the formation of oxygenated sulfur species. In general, weaker signals were observed for LHO-NCM85, due to the presence of a

protective surface shell and the low amount of remaining residual lithium (see also **Fig. S4b** for relative amounts from quantitative XPS analysis). This corroborates the above results and provides clear evidence that the Li_2HfO_3/HfO_2 coating can mitigate but not prevent interfacial degradation, despite good surface coverage. A similar trend was evident from the P 2p data. A new doublet appeared at 133.9 eV (P 2p3/2) that can be assigned primarily to insulating (meta)phosphates.

Finally, electrochemical impedance spectroscopy (EIS) measurements were conducted at 45 °C on the cells after 200 cycles at the end of discharge with the objective to quantitatively determine the different contributions to the resistance. Respective Nyquist plots of the electrochemical impedance are shown in **Fig. 6a**. The equivalent circuit, R_{Bulk}-(R_{GB}/CPE)-($R_{CAM|SE}$/CPE)-CPE, used in the fitting of the EIS data is presented in the inset of **Fig. 6a**. Both bulk (R_{Bulk}) and grain-boundary resistance (R_{GB}) in the high-frequency range were found to be similar for the Bare- and LHO-NCM85 (see **Fig. 6b** and fitting results in **Tab. S4**). However, as expected, a significant difference in cathode interfacial resistance ($R_{CAM|SE}$) in the medium-to-low frequency range was apparent, with ~50 Ω cm^2 for LHO-NCM85 and ~850 Ω cm^2 for Bare-NCM85. This strong impedance rise can only be explained by major differences in the chemomechanics and degradation at interfaces within the cathode.

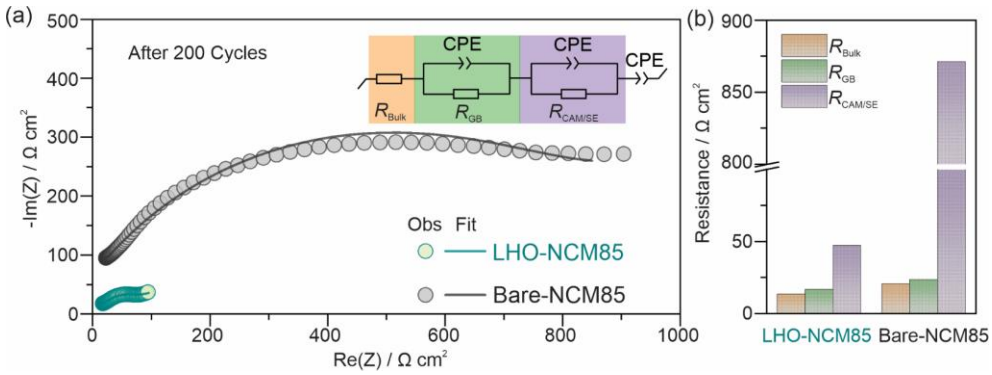

Figure 6. EIS measurements conducted on the pellet-stack SSB full cells with Bare-NCM85 and LHO-NCM85 after 200 cycles at 0.2C. (a) Nyquist plots of the electrochemical impedance and corresponding curve fits, with the equivalent circuit shown in the inset. (b) Comparison of the different resistances.

Conclusions

Using a facile nanoparticle-based coating strategy, this work successfully fabricated a Li_2HfO_3/HfO_2 (LHO) protective coating on the secondary particles of a Ni-rich NCM (NCM85) cathode active material by consumption of residual lithium species during post-deposition annealing. TEM investigations indicated that the hybrid coating is relatively uniform (high surface coverage) and dense and has a thickness of ~12 nm. In sulfide-

based solid-state battery cells, the LHO-coated NCM85 cathode showed superior electrochemical performance in terms of capacity, reversibility, rate capability, and longevity/stability compared to the uncoated counterpart. This improvement results from some stabilization of the interfaces within the cathode, mainly between the cathode active material and the solid electrolyte, and therefore mitigated electro-chemo-mechanical degradation during cycling, as confirmed by various characterization methods such as SEM, XPS, and EIS.

We believe that this work paves the way towards development of lithium-based protective coatings on layered Ni-rich oxide cathode active materials, which are inherently susceptible to formation of lithium surface impurities, and may foster the exploration of novel ionically conductive coatings. In this regard, it should be noted that lithium-containing materials are challenging to prepare as nanoscale (high-quality) coatings.

Experimental Section

Synthesis and Surface Coating

The preparation of HfO_2 NPs and the CAM coating followed previously published procedures.[20,23] In short, hafnium(IV) chloride (≥ 99%, Sigma-Aldrich) was combined with anhydrous benzyl alcohol (≥ 99%, VWR), followed by solvothermal reaction in an autoclave at 250 °C for 3 d. The product formed was washed and then transferred into chloroform (≥ 99%, VWR) for surface functionalization with both oleic acid (≥ 99%, Alfa Aesar) and oleylamine (≥ 99%, Alfa Aesar). The resulting (quasi-transparent) dispersion of concentration ~20 mg(HfO_2)/mL(CH_3Cl) was used for coating the CAM secondary particles. Prior to coating, the NCM85 (BASF SE) was heated in oxygen at 750 °C for 3 h in order to reduce the amount of residual lithium species. A certain volume of the HfO_2 NP dispersion (plus some extra chloroform) was dropwise added to the CAM powder, targeting a coating content of 1 wt. %. Next, the suspension was sonicated for 15 min, followed by heating at 60 °C in an oil bath under magnetic stirring until complete evaporation of the solvent. Finally, the remaining black powder was treated in a vacuum overnight and then heated in oxygen at 700 °C for 2 h. After natural cooling, the LHO-coated NCM85 was transferred into an argon glovebox for further use.

Electrode Preparation

LPSCl (NEI Corp.) and Super C65 (TIMCAL Ltd.) were used as SE and carbon additive, respectively. Ball milling was employed to produce the cathode composite, with the CAM:SE:Super C65 ratio being 69.3:29.7:1.0 by weight. After filling the powder mixture into a 70 mL zirconia jar containing 10 zirconia balls of diameter 10 mm under argon atmosphere (glovebox conditions with H_2O < 0.1 ppm and O_2 < 0.1 ppm), it was milled at 140 rpm for 30 min using a FRITSCH planetary mill. For the anode composite preparation, carbon-coated LTO (NEI Corp.), SE, and Super C65 (30:60:10 by weight) were mixed

under the same conditions as described above for the cathode.

Cell Assembly

A customized cell setup with a PEEK ring of inner diameter 10 mm and two stainless steel dies as current collectors was used in the electrochemical testing of pellet-stack SSBs. 100 mg of SE was packed into the PEEK ring and then compressed at 62 MPa to produce the separator layer. Next, 65 and 12 mg of anode and cathode composite, respectively, was spread onto both sides of the separator. Finally, about 435 MPa was applied for 3 min to ensure proper contact between the different components in the electrode. The assembled cells were finally sealed into pouch bags to prevent exposure to the external atmosphere and (harmful) gas release into the environment.

Electrochemical Testing

The electrochemical performance was tested at different C-rates (1.0C = 190 mA/g) and at 45 °C and 81 MPa using a MACCOR battery cycler. The voltage range was set to 1.35-2.75 V vs. $Li_4Ti_5O_{12}/Li_7Ti_5O_{12}$, which corresponds to about 2.9-4.3 V vs. Li^+/Li. A BioLogic SP-300 potentiostat was used for EIS measurements in the frequency range from 7 MHz to 100 mHz with a voltage amplitude of 7 mV (after a resting period of 1 h at the end of discharge to reach equilibrium).

Physicochemical Characterization

For SEM imaging, a Leo 1530 microscope (Zeiss) equipped with a field emission source was used, and the accelerating voltage was set to 10 kV. EDS was measured using an Oxford X-Max^N detector (Oxford Instruments) at 20 kV.

TEM measurements were performed at an accelerating voltage of 300 kV using a double-corrected Themis-Z microscope (Thermo Fisher Scientific) equipped with a HAADF STEM detector, a Super-X EDS detector, and a Gatan Continuum 970 High-Resolution image filter. The beam current used for STEM EDS mapping was about 200 pA. For TEM lamella preparation, a dual beam focused Ga-ion beam in an FEI Strata 400 at 30 kV was used. The surfaces were protected with carbon coatings by means of ion beam-induced deposition. The samples were subsequently thinned and further cleaned at 5 and 2 kV.

ICP-OES was conducted on samples using an iCAP 7600 DUO (Thermo Fisher Scientific). To this end, CAM powder was digested in a mixture of HCl and H_2SO_4 at 250 °C for 12 h. $HfCl_2O$ (Alfa Aesar) dissolved into 5% HCl was used as standard for Hf calibration.

ATR-IR was measured from 1800 to 600 cm^{-1} using an ALPHA FT-IR spectrometer (Bruker).

For XRD measurements, samples were packed into 0.5 mm borosilicate capillaries (Hilgenberg), and data were acquired in Debye-Scherrer geometry using a STOE Stadi-P diffractometer equipped with a Mo anode and a DECTRIS MYTHEN 1K strip detector. The instrumental contribution to peak broadening was determined by measuring a NIST

Si 640f standard reference material as line broadening reference. Rietveld refinement was performed using GSAS-II.[56] For refinement of NCM structural models against the diffraction data, the scale factor, zero shift, and size/strain broadening parameters were allowed to vary. A fixed background was fitted to the data using a Chebyshev polynomial function with 13 terms. In the structural model, the cell parameters, oxygen *z* coordinate, and atomic displacement parameters for each site were refined. Atoms occupying the same site were constrained to have the same atomic parameters, and site occupancy factors were constrained such that each site remained fully occupied.

XPS measurements were performed on a SPECS system with a PHOIBOS 150 energy analyzer using monochromatic Al-Kα radiation. Takeoff angle and pass energies for detail and survey scans were set to 45° and 30/90 eV, respectively. The C 1s peak of adventitious carbon at 284.8 eV was used for binding energy calibration. Curve fits were done with the CasaXPS software using mixed Gaussian-Lorentzian peak functions and Shirley-type backgrounds. The peak area ratio and spin-orbit splitting were set to 4:3 and 1.71 eV for the Hf 4f features, while a 2:1 ratio and splitting of 0.84 and 1.18 eV were used to describe the P 2p and S 2p peak doublets, respectively.[57]

Conflicts of Interest

The authors declare no competing financial interest.

Supporting Information

The Supporting Information is available free of charge at…

XRD pattern and Rietveld refinement profile for Bare-NCM85; rate performance data for the Bare- and LHO-NCM85-based cells; differential capacity curves; S 2p and P 2p XP spectra and relative amounts of sulfur and phosphorus species; tables detailing the refined structural parameters, the relative percentage of Hf species with different chemical environments, the ICP-OES results, and the EIS fitting results; discussion on the chemical reaction(s) leading to Li_2HfO_3 formation.

Acknowledgements

This study was supported by BASF SE. The authors acknowledge Dr. Thomas Bergfeldt (Institute for Applied Materials – Applied Materials Physics, KIT) for assistance with the ICP-OES measurements. Y.T. acknowledges financial support from the German Research Foundation (DFG) under project ID 390874152 (POLiS Cluster of Excellence).

References

1. Janek, J.; Zeier, W. G., Challenges in Speeding Up Solid-State Battery Development. *Nat. Energy* **2023**, *8*, 230-240.

2. Zhao, Q.; Stalin, S.; Zhao, C.-Z.; Archer, L. A., Designing Solid-State Electrolytes for Safe, Energy-Dense Batteries. *Nat. Rev. Mater.* **2020**, *5*, 229-252.

3. Zhang, Q.; Cao, D.; Ma, Y.; Natan, A.; Aurora, P.; Zhu, H., Sulfide-Based Solid-State Electrolytes: Synthesis, Stability, and Potential for All-Solid-State Batteries. *Adv. Mater.* **2019**, *31*, 1901131.

4. Niu, C.; Lee, H.; Chen, S.; Li, Q.; Du, J.; Xu, W.; Zhang, J.-G.; Whittingham, M. S.; Xiao, J.; Liu, J., High-Energy Lithium Metal Pouch Cells with Limited Anode Swelling and Long Stable Cycles. *Nat. Energy* **2019**, *4*, 551-559.

5. Ma, Y.; Ma, Y.; Geiger, D.; Kaiser, U.; Zhang, H.; Kim, G.-T.; Diemant, T.; Behm, R. J.; Varzi, A.; Passerini, S., ZnO/$ZnFe_2O_4$/N-Doped C Micro-Polyhedrons with Hierarchical Hollow Structure as High-Performance Anodes for Lithium-Ion Batteries. *Nano Energy* **2017**, *42*, 341-352.

6. Li, W.; Song, B.; Manthiram, A., High-Voltage Positive Electrode Materials for Lithium-Ion batteries. *Chem. Soc. Rev.* **2017**, *46*, 3006-3059.

7. Zhou, L.; Park, K.-H.; Sun, X.; Lalère, F.; Adermann, T.; Hartmann, P.; Nazar, L. F., Solvent-Engineered Design of Argyrodite Li_6PS_5X (X = Cl, Br, I) Solid Electrolytes with High Ionic Conductivity. *ACS Energy Lett.* **2019**, *4*, 265-270.

8. Shin, B. R.; Nam, Y. J.; Oh, D. Y.; Kim, D. H.; Kim, J. W.; Jung, Y. S., Comparative Study of TiS_2/Li-In All-Solid-State Lithium Batteries Using Glass-Ceramic Li_3PS_4 and $Li_{10}GeP_2S_{12}$ Solid Electrolytes. *Electrochim. Acta* **2014**, *146*, 395-402.

9. Yamane, H.; Shibata, M.; Shimane, Y.; Junke, T.; Seino, Y.; Adams, S.; Minami, K.; Hayashi, A.; Tatsumisago, M., Crystal Structure of a Superionic Conductor, $Li_7P_3S_{11}$. *Solid State Ionics* **2007**, *178*, 1163-1167.

10. Kato, Y.; Hori, S.; Saito, T.; Suzuki, K.; Hirayama, M.; Mitsui, A.; Yonemura, M.; Iba, H.; Kanno, R., High-Power All-Solid-State Batteries Using Sulfide Superionic Conductors. *Nat. Energy* **2016**, *1*, 16030.

11. Karger, L.; Weber, D.; Goonetilleke, D.; Mazilkin, A.; Li, H.; Zhang, R.; Ma, Y.; Indris, S.; Kondrakov, A.; Janek, J.; Brezesinski, T., Low-Temperature Ion Exchange Synthesis of Layered $LiNiO_2$ Single Crystals with High Ordering. *Chem. Mater.* **2023**, *35*, 648-657.

12. Zhu, Y.; He, X.; Mo, Y., Origin of Outstanding Stability in the Lithium Solid Electrolyte Materials: Insights from Thermodynamic Analyses Based on First-Principles Calculations. *ACS Appl. Mater. Interfaces* **2015**, *7*, 23685-23693.

13. Richards, W. D.; Miara, L. J.; Wang, Y.; Kim, J. C.; Ceder, G., Interface Stability in Solid-State Batteries. *Chem. Mater.* **2016**, *28*, 266-273.

14. Dewald, G. F.; Ohno, S.; Kraft, M. A.; Koerver, R.; Till, P.; Vargas-Barbosa, N. M.; Janek, J.; Zeier, W. G., Experimental Assessment of the Practical Oxidative Stability of Lithium Thiophosphate Solid Electrolytes. *Chem. Mater.* **2019**, *31*, 8328-8337.

15. Li, X.; Ren, Z.; Norouzi Banis, M.; Deng, S.; Zhao, Y.; Sun, Q.; Wang, C.; Yang, X.; Li, W.; Liang, J.; Li, X.; Sun, Y.; Adair, K.; Li, R.; Hu, Y.; Sham, T.-K.; Huang, H.; Zhang, L.; Lu, S.; Luo, J.; Sun, X., Unravelling the Chemistry and Microstructure Evolution of a Cathodic Interface in Sulfide-Based All-Solid-State Li-Ion Batteries. *ACS Energy Lett.* **2019**, *4*, 2480-2488.

16. Kobayashi, S.; Watanabe, H.; Kato, T.; Mizuno, F.; Kuwabara, A., Atomic-Scale Observations of Oxygen Release Degradation in Sulfide-Based All-Solid-State Batteries with Layered Oxide Cathodes. *ACS Appl. Mater. Interfaces* **2022**, *14*, 39459-39466.

17. Zuo, T.-T.; Ruess, R.; Pan, R.; Walther, F.; Rohnke, M.; Hori, S.; Kanno, R.; Schroder, D.; Janek, J., A Mechanistic Investigation of the $Li_{10}GeP_2S_{12}$|$LiNi_{1-x-y}Co_xMn_yO_2$ Interface Stability in All-Solid-State Lithium Batteries. *Nat. Commun.* **2021**, *12*, 6669.

18. Song, Y. B.; Kwak, H.; Cho, W.; Kim, K. S.; Jung, Y. S.; Park, K.-H., Electrochemo-Mechanical Effects as a Critical Design Factor for All-Solid-State Batteries. *Curr. Opin. Solid State Mater. Sci.* **2022**, *26*, 100977.

19. Minnmann, P.; Strauss, F.; Bielefeld, A.; Ruess, R.; Adelhelm, P.; Burkhardt, S.; Dreyer, S. L.; Trevisanello, E.; Ehrenberg, H.; Brezesinski, T.; Richter, F. H.; Janek, J., Designing Cathodes and Cathode Active Materials for Solid-State Batteries. *Adv. Energy Mater.* **2022**, *12*, 2201425.

20. Ma, Y.; Teo, J. H.; Walther, F.; Ma, Y.; Zhang, R.; Mazilkin, A.; Tang, Y.; Goonetilleke, D.; Janek, J.; Bianchini, M.; Brezesinski, T., Advanced Nanoparticle Coatings for Stabilizing Layered Ni-Rich Oxide Cathodes in Solid-State Batteries. *Adv. Funct. Mater.* **2022**, *32*, 2111829.

21. Kitsche, D.; Tang, Y.; Hemmelmann, H.; Walther, F.; Bianchini, M.; Kondrakov, A.; Janek, J.; Brezesinski, T., Atomic Layer Deposition Derived Zirconia Coatings on Ni-Rich Cathodes in Solid-State Batteries: Correlation Between Surface Constitution and Cycling Performance. *Small Sci.* **2023**, *3*, 2200073.

22. Kitsche, D.; Tang, Y.; Ma, Y.; Goonetilleke, D.; Sann, J.; Walther, F.; Bianchini, M.; Janek, J.; Brezesinski, T., High Performance All-Solid-State Batteries with a Ni-

Rich NCM Cathode Coated by Atomic Layer Deposition and Lithium Thiophosphate Solid Electrolyte. *ACS Appl. Energy Mater.* **2021**, *4*, 7338-7345.

23. Ma, Y.; Zhang, R.; Tang, Y.; Ma, Y.; Teo, J. H.; Diemant, T.; Goonetilleke, D.; Janek, J.; Bianchini, M.; Kondrakov, A.; Brezesinski, T., Single- to Few-Layer Nanoparticle Cathode Coating for Thiophosphate-Based All-Solid-State Batteries. *ACS Nano* **2022**, *16*, 18682-18694.

24. Woo, J. H.; Trevey, J. E.; Cavanagh, A. S.; Choi, Y. S.; Kim, S. C.; George, S. M.; Oh, K. H.; Lee, S.-H., Nanoscale Interface Modification of $LiCoO_2$ by Al_2O_3 Atomic Layer Deposition for Solid-State Li Batteries. *J. Electrochem. Soc.* **2012**, *159*, A1120-A1124.

25. Sakuda, A.; Kitaura, H.; Hayashi, A.; Tadanaga, K.; Tatsumisago, M., All-Solid-State Lithium Secondary Batteries with Oxide-Coated $LiCoO_2$ Electrode and Li_2S–P_2S_5 Electrolyte. *J. Power Sources* **2009**, *189*, 527-530.

26. Lee, Y.-G.; Fujiki, S.; Jung, C.; Suzuki, N.; Yashiro, N.; Omoda, R.; Ko, D.-S.; Shiratsuchi, T.; Sugimoto, T.; Ryu, S.; Ku, J. H.; Watanabe, T.; Park, Y.; Aihara, Y.; Im, D.; Han, I. T., High-Energy Long-Cycling All-Solid-State Lithium Metal Batteries Enabled by Silver–Carbon Composite Anodes. *Nat. Energy* **2020**, *5*, 299-308.

27. Payandeh, S.; Strauss, F.; Mazilkin, A.; Kondrakov, A.; Brezesinski, T., Tailoring the $LiNbO_3$ Coating of Ni-Rich Cathode Materials for Stable and High-Performance All-Solid-State Batteries. *Nano Res. Energy* **2022**, *1*, e9120016.

28. Kim, Y.-J.; Rajagopal, R.; Kang, S.; Ryu, K.-S., Novel Dry Deposition of $LiNbO_3$ or Li_2ZrO_3 on $LiNi_{0.6}Co_{0.2}Mn_{0.2}O_2$ for High Performance All-Solid-State Lithium Batteries. *Chem. Eng. J.* **2020**, *386,* 123975.

29. Negi, R. S.; Yusim, Y.; Pan, R.; Ahmed, S.; Volz, K.; Takata, R.; Schmidt, F.; Henss, A.; Elm, M. T., A Dry-Processed Al_2O_3/$LiAlO_2$ Coating for Stabilizing the Cathode/Electrolyte Interface in High-Ni NCM-Based All-Solid-State Batteries. *Adv. Mater. Interfaces* **2022**, *9*, 2101428.

30. Strauss, F.; Teo, J. H.; Maibach, J.; Kim, A-Y.; Mazilkin, A.; Janek, J.; Brezesinski, T., Li_2ZrO_3-Coated NCM622 for Application in Inorganic Solid-State Batteries: Role of Surface Carbonates in the Cycling Performance. *ACS Appl. Mater. Interfaces* **2020**, *12*, 57146-57154.

31. Ohta, N.; Takada, K.; Zhang, L.; Ma, R.; Osada, M.; Sasaki, T., Enhancement of the High-Rate Capability of Solid-State Lithium Batteries by Nanoscale Interfacial Modification. *Adv. Mater.* **2006**, *18*, 2226-2229.

32. Kim, A-Y.; Strauss, F.; Bartsch, T.; Teo, J. H.; Hatsukade, T.; Mazilkin, A.; Janek, J.; Hartmann, P.; Brezesinski, T., Stabilizing Effect of a Hybrid Surface Coating on

a Ni-Rich NCM Cathode Material in All-Solid-State Batteries. *Chem. Mater.* **2019**, *31*, 9664-9672.

33. Jung, S. H.; Oh, K.; Nam, Y. J.; Oh, D. Y.; Brüner, P.; Kang, K.; Jung, Y. S., Li_3BO_3–Li_2CO_3: Rationally Designed Buffering Phase for Sulfide All-Solid-State Li-Ion Batteries. *Chem. Mater.* **2018**, *30*, 8190-8200.

34. Strauss, F.; Teo, J. H.; Schiele, A.; Bartsch, T.; Hatsukade, T.; Hartmann, P.; Janek, J.; Brezesinski, T., Gas Evolution in Lithium-Ion Batteries: Solid versus Liquid Electrolyte. *ACS Appl. Mater. Interfaces* **2020**, *12*, 20462-20468.

35. Mahne, N.; Renfrew, S. E.; McCloskey, B. D.; Freunberger, S. A., Electrochemical Oxidation of Lithium Carbonate Generates Singlet Oxygen. *Angew. Chem., Int. Ed.* **2018**, *57*, 5529-5533.

36. Nolan, A. M.; Liu, Y.; Mo, Y., Solid-State Chemistries Stable with High-Energy Cathodes for Lithium-Ion Batteries. *ACS Energy Lett.* **2019**, *4* , 2444-2451.

37. Nolan, A. M.; Wachsman, E. D.; Mo, Y., Computation-Guided Discovery of Coating Materials to Stabilize the Interface Between Lithium Garnet Solid Electrolyte and High-Energy Cathodes for All-Solid-State Lithium Batteries. *Energy Storage Mater.* **2021**, *41*, 571-580.

38. Busca, G.; Lorenzelli, V., Infrared Spectroscopic Identification of Species Arising from Reactive Adsorption of Carbon Oxides on Metal Oxide Surfaces. *Mater. Chem.* **1982**, *7*, 89-126.

39. Nand, M.; Rajput, P.; Choudhary, R. J.; Jha, S. N., Effect of Y_2O_3 Doping on HfO_2 Thin Film Prepared by Pulsed Laser Deposition (PLD): XPS Studies. *AIP Conf. Proc.* **2019**, *2115*, 030330.

40. Lu, Q.; Huang, R.; Lan, X.; Chi, X.; Lu, C.; Li, C.; Wu, Z.; Li, J.; Han, G.; Yan, P., Amazing Diffusion Depth of Ultra-Thin Hafnium Oxide Film Grown on n-Type Silicon by Lower Temperature Atomic Layer Deposition. *Mater. Lett.* **2016**, *169*, 164-167.

41. Negi, R. S.; Celik, E.; Pan, R.; Stäglich, R.; Senker, J.; Elm, M. T., Insights into the Positive Effect of Post-Annealing on the Electrochemical Performance of Al_2O_3-Coated Ni-Rich NCM Cathodes for Lithium-Ion Batteries. *ACS Appl. Energy Mater.* **2021**, *4*, 3369-3380.

42. Schipper, F.; Bouzaglo, H.; Dixit, M.; Erickson, E. M.; Weigel, T.; Talianker, M.; Grinblat, J.; Burstein, L.; Schmidt, M.; Lampert, J.; Erk, C.; Markovsky, B.; Major, D. T.; Aurbach, D., From Surface ZrO_2 Coating to Bulk Zr Doping by High Temperature Annealing of Nickel-Rich Lithiated Oxides and Their Enhanced Electrochemical Performance in Lithium Ion Batteries. *Adv. Energy Mater.* **2018**, *8*, 1701682.

43. Jain, A.; Ong, S. P.; Hautier, G.; Chen, W.; Richards, W. D.; Dacek, S.; Cholia, S.; Gunter, D.; Skinner, D.; Ceder, G.; Persson, K. A., Commentary: The Materials Project: A Materials Genome Approach to Accelerating Materials Innovation. *APL Mater.* **2013**, *1*, 011002.

44. Taguchi, N.; Sakaebe, H.; Tatsumi, K.; Akita, T., Degradation Analysis of $LiCoO_2$ Positive Electrode Material of a Li-Ion Battery Using the Li K-Edge Signal Obtained from STEM-EELS Measurements. *e-J. Surf. Sci. Nanotechnol.* **2015**, *13*, 284-288.

45. Cheynet, M. C.; Pokrant, S.; Tichelaar, F. D.; Rouvière, J.-L., Crystal Structure and Band Gap Determination of HfO_2 Thin Films. *J. Appl. Phys.* **2007**, *101*, 054101.

46. Ahn, C. C.; Krivanek, O. L., EELS Atlas: A Reference Guide of Electron Energy Loss Spectra Covering all Stable Elements, Gatan Inc., 1983.

47. Ma, Y.; Teo, J. H.; Kitsche, D.; Diemant, T.; Strauss, F.; Ma, Y.; Goonetilleke, D.; Janek, J.; Bianchini, M.; Brezesinski, T., Cycling Performance and Limitations of $LiNiO_2$ in Solid-State Batteries. *ACS Energy Lett.* **2021**, *6*, 3020-3028.

48. Shi, T.; Zhang, Y.-Q.; Tu, Q.; Wang, Y.; Scott, M. C.; Ceder, G., Characterization of Mechanical Degradation in an All-Solid-State Battery Cathode. *J. Mater. Chem. A* **2020**, *8*, 17399-17404.

49. Zuo, T.-T.; Walther, F.; Ahmed, S.; Rueß, R.; Hertle, J.; Mogwitz, B.; Volz, K.; Janek, J., Formation of an Artificial Cathode–Electrolyte Interphase to Suppress Interfacial Degradation of Ni-Rich Cathode Active Material with Sulfide Electrolytes for Solid-State Batteries. *ACS Energy Lett.* **2023**, *8*, 1322-1329.

50. Payandeh, S.; Njel, C.; Mazilkin, A.; Teo, J. H.; Ma, Y.; Zhang, R.; Kondrakov, A.; Bianchini, M.; Brezesinski, T., The Effect of Single versus Polycrystalline Cathode Particles on All-Solid-State Battery Performance. *Adv. Mater. Interfaces* **2023**, *10*, 2201806.

51. Han, Y.; Jung, S. H.; Kwak, H.; Jun, S.; Kwak, H. H.; Lee, J. H.; Hong, S.-T.; Jung, Y. S., Single- or Poly-Crystalline Ni-Rich Layered Cathode, Sulfide or Halide Solid Electrolyte: Which Will be the Winners for All-Solid-State Batteries? *Adv. Energy Mater.* **2021**, *11*, 2100126.

52. Zhang, R.; Strauss, F.; Jiang, L.; Casalena, L.; Li, L.; Janek, J.; Kondrakov, A.; Brezesinski, T., Transition-Metal Interdiffusion and Solid Electrolyte Poisoning in All-Solid-State Batteries Revealed by Cryo-TEM. *Chem. Commun.* **2023**, *59*, 4600-4603.

53. Zhang, X.; Wang, Z.; Li, X.; Su, Y.; Ye, Z.; Zhang, L.; Huang, Q.; Tang, Y.; Huang, J., Assessing the Roles of Mechanical Cracks in Ni-Rich Layered Cathodes in the Capacity Decay of Liquid and Solid-State Batteries. *Mater. Horiz.* **2023**, *10*, 1856-1864.

54. Walther, F.; Strauss, F.; Wu, X.; Mogwitz, B.; Hertle, J.; Sann, J.; Rohnke, M.; Brezesinski, T.; Janek, J., The Working Principle of a Li_2CO_3/$LiNbO_3$ Coating on NCM for Thiophosphate-Based All-Solid-State Batteries. *Chem. Mater.* **2021**, *33*, 2110-2125.

55. Auvergniot, J.; Cassel, A.; Foix, D.; Viallet, V.; Seznec, V.; Dedryvère, R., Redox Activity of Argyrodite Li_6PS_5Cl Electrolyte in All-Solid-State Li-Ion Battery: An XPS Study. *Solid State Ionics* **2017**, *300*, 78-85.

56. Toby, B. H.; Von Dreele, R. B., GSAS-II: The Genesis of a Modern Open-Source All Purpose Crystallography Software Package. *J. Appl. Crystallogr.* **2013**, *46*, 544-549.

57. Moulder, J. F.; Stickle, W. F.; Sobol, P. E.; Bomben, K. D., Handbook of X-ray Photoelectron Spectroscopy, Perkin Elmer Corp., Eden Prairie, MN, USA, 1992.

TOC Graphic

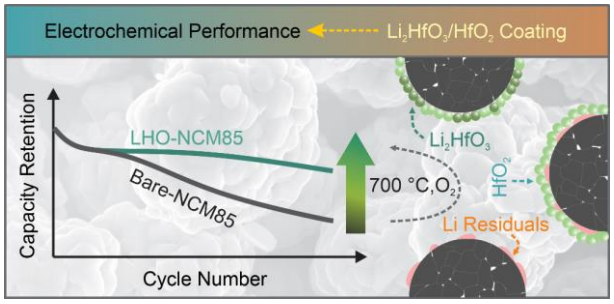
Electrochemical Performance
Li2HfO3/HfO2 Coating
Capacity Retention
Cycle Number
LHO-NCM85
Bare-NCM85
700 °C,O2
Li2HfO3
HfO2
Li Residuals